Research Article

Shuguang Li*, Kashif Ali, Salem Algarni, Talal Alqahtani, Sohail Ahmad, Fayza Abdel Aziz ElSeabee, Hameed Ullah, Wasim Jamshed, and Kashif Irshad

Numerical analysis of thermophoretic particle deposition in a magneto-Marangoni convective dusty tangent hyperbolic nanofluid flow – Thermal and magnetic features

https://doi.org/10.1515/ntrev-2023-0190
received April 30, 2023; accepted December 21, 2023

Abstract: In the current study, we focus on the Magneto-Marangoni convective flow of dusty tangent hyperbolic nanofluid (TiO_2 – kerosene oil) over a sheet in the presence of thermophoresis particles deposition and gyrotactic microorganisms. Along with activation energy, heat source, variable viscosity, and thermal conductivity, the Dufour-Soret effects are taken into consideration. Variable surface tension gradients are used to identify Marangoni convection. Melting of drying wafers, coating flow technology, wielding, crystals, soap film stabilization, and microfluidics all depend on Marangoni driven flow. This study's major objective is to ascertain the thermal mobility of nanoparticles in a fluid with a kerosene oil base. To improve mass transfer phenomena, we inserted microorganisms into the base fluid. By using similarity transformations, the resulting system of nonlinear partial differential equations is converted into nonlinear ordinary differential equations. Using a shooting technique based on RKF-45th order, the numerical answers are obtained. For various values of the physical parameters, the local density of motile microorganisms, Nusselt number, skin friction, and Sherwood number are calculated. The findings demonstrated that as the Marangoni convection parameter is raised, the velocity profiles of the dust and fluid phases increase, but the microorganisms, concentration, and temperature profiles degrade in both phases.

Keywords: numerical methods, Dufour-Soret effects, Marangoni convection, gyrotactic microorganisms, thermophoretic particle deposition, dusty tangent hyperbolic nanofluid, nonlinear equations

*** Corresponding author: Shuguang Li,** School of Computer Science and Technology, Shandong Technology and Business University, Yantai, 264005, China, e-mail: shuguangli2023@hotmail.com, sgliytu@hotmail.com
Kashif Ali, Sohail Ahmad: Department of Basic Sciences and Humanities, Muhammad Nawaz Sharif University of Engineering and Technology, Multan, 60000, Pakistan
Salem Algarni, Talal Alqahtani: Mechanical Engineering Department, College of Engineering, King Khalid University, Abha 9004, Saudi Arabia
Fayza Abdel Aziz ElSeabee: Department of Mathematics, College of Science and Arts, Qassim University, Alasyah, 51971, Saudi Arabia; Mathematics Department, Faculty of Science, Helwan University, Cairo, Egypt
Hameed Ullah: Department of Mathematics, COMSATS University Islamabad, Sahiwal Campus, Sahiwal, 57000, Pakistan
Wasim Jamshed: Department of Mathematics, Capital University of Science & Technology, Islamabad, 44000, Pakistan; Mathematics in Applied Sciences and Engineering Research Group, Scientific Research Center, Al-Ayen University, Nasiriyah, 64001, Iraq
Kashif Irshad: Interdisciplinary Research Centre for Sustainable Energy Systems (IRC-SES), Research Institute, King Fahd University of Petroleum and Minerals (KFUPM), Dhahran, 31261, Saudi Arabia

Nomenclature

C_p	specific heat of the fluid (Jkg^{-1} k^{-1})
ϵ	variable thermal conductivity parameter
ϵ_1	variable viscosity parameter
Ec	Eckert number
M	magnetic parameter
$K = 6\pi\mu r$	coefficient of drag Stokes
Pe	bioconvection Peclet number
Pr	Prandtl number
q_r	radiative heat flux (kW/m^2)
r	radius of the dust particle
U_e	free stream velocity (m s^{-1})
(u_p, v_p)	velocity fields of particle phase (m s^{-1})
ν_f	kinematic viscosity (m^2 s^{-1})
W_c	maximum cell swimming speed
We	Weissenberg number
β_c	parameter for fluid–particle interaction for concentration

τ_v	relaxation time of the dust particles
ρ_P	particle density
τ_m	time required by the motile organisms
Γ	time constant
τ_v	momentum relaxation time
τ_T	thermal relaxation time
ρ_f	fluid density (kg/m^3)
$\psi(x, y)$	streams functions of fluid phase
σ	surface tension (N/m)
β_m	fluid–particle interaction parameter for bioconvection
σ_0	surface tension
β_T	thermal dust parameter
γ	specific heat ratio
β_v	fluid–particle interaction parameter
τ_w	surface shear stress
Ma	Marangoni ratio parameter
Φ	volume fraction of TiO_2
τ	thermophorotic parameter
σ^*	Stefan–Boltzmann constant (W/m^2 K^4)
γ_T	surface tension coefficients for temperature N/m
γ_C	surface tension coefficients for concentration
δ	temperature difference parameter
μ_f	dynamic viscosity (kg m^{-1} s^{-1})
σ_f	electrical conductivity (S m^{-1})
B_0	uniform magnetic field (kg s^{-2} A^{-1})
C	fluid phase concentration
C_{fx}	skin friction
C_m	specific heat of the dust particle
C_p	particle phase concentration
D_m	mass diffusivity coefficient (m^2 s^{-1})
D_n	diffusivity of microorganisms (m^2 s^{-1})
Du	Dufour number
E_a	activation energy coefficient (kg m^2 s^{-2})
k_1	thermophoretic coefficient (m s^{-1} K^{-1})
k_f	thermal conductivity of the fluid (Wm^{-1} K^{-1})
k_r	reaction rate
k^*	mean absorption coefficient (cm^{-1})
L	reference length (m)
Lb	bioconvection Lewis number
Le	Lewis number
n	Power law index
N^*	dimensions of dust particle density
N	density of motile microorganism (kg m^{-3})
Nn_x	local density of motile microorganisms
N_p	density particle phase (kg m^{-3})
Nu_x	Nusselt number
Q_0	heat source (temperature dependent) coefficient
Q_t	temperature dependent heat source parameter
q_w	heat flux $\left(\frac{W}{m^2}\right)$
Rc	chemical reaction parameter
r_P	radius of dust particles (nm)
Sh_x	Sherwood number
Sr	Soret number
T	fluid temperature (K)
T_P	particle temperature (K)
T_{ref}	reference temperature (K)
(u, v)	velocity fields of fluid (m s^{-1})
V_T	thermophoretic velocity (m s^{-1})
(x, y)	Cartesian coordinates (m)
$\Psi(x, y)$	streams functions of dust phase
Ω	microorganisms concentration difference parameter

Superscripts

$'$	derivative with respect to ξ
∞	ambient
nf	nanofluid
f	base fluid

1 Introduction

Non-Newtonian fluids are employed more frequently in engineering and manufacturing processes than Newtonian fluids. The tangent hyperbolic model was one of the non-Newtonian models that Pop and Ingham [1] proposed. The tangent hyperbolic fluid model may well explain the shear thinning phenomenon. Blood, ketchup, paint, and other chemicals are a few examples of fluids with this property. Akbar [2] investigated the tangent hyperbolic fluid's peristaltic flow with convective boundary conditions. Naseer *et al.* [3] investigated the hyperbolic tangent fluid flow in a boundary layer over an exponentially extending vertical cylinder. Salahuddin *et al.*'s [4] examination of tangent hyperbolic fluid flow on stretched surfaces looked at the effects of heat production and absorption.

The nanofluid principle is created by the integration of nanoparticles (1–100 nm) with base liquids. Nanoparticles are usually recommended for enhancing the heating rate in various industrial and technical systems. Choi [5] provided the first analysis of nanofluids using experimental

assumptions and data. Numerous academics have researched the flow of nanofluids over different geometries [6–9].

Many complicated engineering issues, including combustion, rain erosion, waste water treatment, lunar ash flows, paint spraying, corrosive particles in motor oil flow, nuclear reactors, polymer technologies, *etc.*, involve the phenomenon of fluid flow including millimeter-sized dust particles. Saffman [10] provided an inquiry on fluid particle suspension and the stability of laminar flow of dusty fluid. Agranat [11] explored how pressure gradient impacts the rate of heat transmission in a fluid containing dust particles. The safety of nuclear reactors, gas cleaning, micro contamination management, and heat exchanger corrosion are only a few applications of the thermophoresis phenomenon in industry and micro-engineering. This phenomenon happens when a mixture of several movable particle kinds is exposed to a temperature variation.

Different particle kinds respond in different ways. Thermophoresis allows microparticles to move away from warm surfaces and deposit on cool surfaces. The thermophoretic force is the force that the temperature difference has on the suspended particles. The thermophoretic velocity of a particle is its rate of motion. Thermophoresis particle deposition on a wedge-shaped forced convective heat and mass transfer flow in two dimensions with variable viscosity was analyzed by Rahman *et al.* [12]. Abbas *et al.* investigated the deposition of thermophoretic particles in Carreau-Yasuda fluid on a chemically reactive Riga plate [13]. According to the studies [14–16], particle deposition has a considerable impact on liquid flow.

The word "bioconvection" refers to a phenomenon brought on by microorganisms. These bacteria have a propensity to accumulate at the upper section of the fluid, which becomes unstable, as a result of the strong density stratification. When exposed to an external stimulus, moveable microorganisms in the base fluid move in a certain direction, increasing the density of the base fluid. Mobile microorganisms boost the mass transfer rate of species in the solution and have industrial uses in enzyme biosensors, chemical processing, polymer sheets, and biotechnological research. The radiative flow of the Casson fluid *via* a rotating wedge containing gyrotactic microorganisms was studied by Raju *et al.* [17]. For more information, check previous literature [9,18–23].

The Marangoni convective transport mechanism commonly manifests when the liquid–liquid or liquid–air interface surface tension varies on the concentration or the temperature distribution. The study of mass and heat transfer in this phenomenon has garnered a lot of interest due to its numerous applications in the fields of nanotechnology, welding processes, atomic reactors, silicon wafers, thin film stretching, soap films, melting, semiconductor processing, crystal growth, and materials sciences. Kairi *et al.* [24] investigated the effect of the thermosolutal Marangoni on bioconvection in suspension of gyrotactic microorganisms over an inclined stretched sheet. Roy *et al.* [25] studied a non-Newtonian nanofluid thermosolutal Marangoni bioconvection in a stratified environment. The role that Marangoni convective flow plays in the passage of mass and heat into diverse systems was carefully explored in the previous literature [26–31].

The innovative aspect of the current study is the examination of the importance of Marangoni convective flow of magnetized dusty tangent hyperbolic nanofluid over sheet in the presence of thermophoresis particle deposition and gyrotactic microorganisms. Due to the inspiration provided by the aforementioned investigations and uses, the activation energy, heat source, and Soret and Dufour effects have also been discussed. According to the material mentioned above, the current test is brand-new and has not yet been studied. With the help of the RKF-45th method, the resulting problem is numerically solved, and the effects of the pertinent parameters on the distributions of temperature, solutal, velocity, microbes, local skin friction, Sherwood number, and Nusselt number have been carefully analyzed. In order to provide details, the current study addresses the following inquiries:

- What impact do the Weissenberg number and power law index parameter have on the temperature and velocity profiles?
- How do the temperature, microbe concentration, and velocity profiles for the fluid (phase-I) and particle (phase-II) phases change as a result of Marangoni convection?
- What impact does the parameter for nanoparticle volume fraction have on the thermal and velocity profiles?
- What effects do thermophoretic and chemical reaction parameters have on concentration profiles?

What effects do Dufour and Soret numbers have on the profiles of temperature and concentration?

2 Description of the model

We have looked into the Marangoni convection-affected flow of dusty tangent hyperbolic nanofluid over a sheet at $y = 0$ close to a stagnation point. Given that the flow is constrained to the region $y \geq 0$, the coordinates x and y are taken perpendicularly and vertically to the flow, respectively. We consider the free stream velocity to be $U_e(x) = ex$. In Figure 1, the problem's configuration is shown. Along

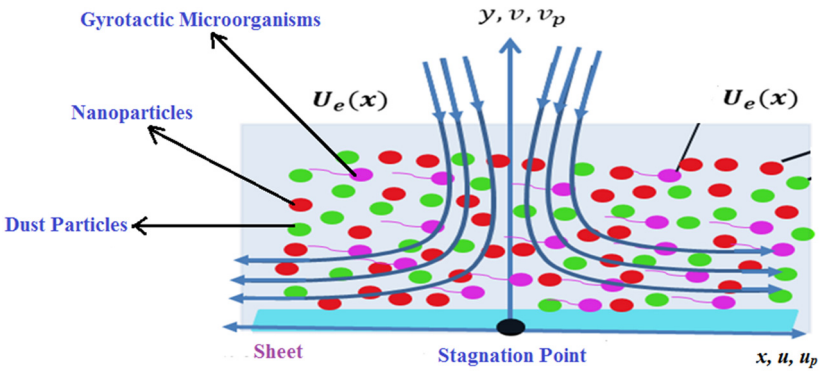

Figure 1: Problem description.

the y-axis, a magnetic field with constant strength B_0 is applied. TiO_2 in kerosene oil is used to determine its thermal properties and correlations. Gyrotactic bacteria and thermophoresis particle deposition are taken into consideration. It is assumed that the sphere-shaped dust and nanoparticles were evenly dispersed throughout the fluid.

2.1 Governing equations

The model equations for both phases are given below ([32,33]):

First phase (for fluid):

$$\frac{\partial u}{\partial x} + \frac{\partial v}{\partial y} = 0, \tag{1}$$

$$\rho_{\mathrm{nf}}\left(u\frac{\partial u}{\partial x} + v\frac{\partial u}{\partial y}\right) = \frac{\partial}{\partial y}\left[\mu^*(T)\left((1-n)\frac{\partial u}{\partial y} + \sqrt{2}n\Gamma\left(\frac{\partial u}{\partial y}\right)^2\right)\right] + U_{\mathrm{e}}\frac{\partial U_{\mathrm{e}}}{\partial x} + \frac{\rho_{\mathrm{p}}}{\tau_{\mathrm{v}}}(u_{\mathrm{p}} - u) + \sigma_{\mathrm{nf}}B_0^2(U_{\mathrm{e}} - u), \tag{2}$$

$$(\rho c_{\mathrm{p}})_{\mathrm{nf}}\left(u\frac{\partial T}{\partial x} + v\frac{\partial T}{\partial y}\right) = \frac{\partial}{\partial y}\left(K^*(T)\frac{\partial T}{\partial y}\right) - \frac{\partial}{\partial y}(q_{\mathrm{r}}) + \frac{\rho_{pC_{\mathrm{m}}}}{\tau_{\mathrm{t}}}(T_{\mathrm{p}} - T) + \frac{\rho_{\mathrm{p}}}{\tau_{\mathrm{v}}}(u_{\mathrm{p}} - u)^2 + (\mu^*(T))\left((1-n) + \frac{n\Gamma}{\sqrt{2}}\frac{\partial u}{\partial y}\right)\left(\frac{\partial u}{\partial y}\right)^2 + \left(\frac{D_{\mathrm{m}}k_{\mathrm{T}}}{C_{\mathrm{s}}}\right)\frac{\partial^2 C}{\partial y^2} + Q_0(T - T_\infty) + Q_1(T_{\mathrm{w}} - T_\infty)e^{\left(-my\sqrt{\frac{d}{v_f}}\right)}, \tag{3}$$

$$u\frac{\partial C}{\partial x} + v\frac{\partial C}{\partial y} = D_{\mathrm{m}}\frac{\partial^2 C}{\partial y^2} + \frac{\rho_{\mathrm{p}}}{\rho\tau_C}(C_{\mathrm{p}} - C) + \frac{D_{\mathrm{m}}k_{\mathrm{T}}}{T_{\mathrm{m}}}\frac{\partial^2 T}{\partial y^2} - \frac{\partial}{\partial y}\left(-\frac{k_1 v}{T_{\mathrm{ref}}}\frac{\partial T}{\partial y}(C - C_\infty)\right) - k_{\mathrm{r}}^2(C - C_\infty)\left(\frac{T}{T_\infty}\right)^{\mathrm{m}}\exp\left(\frac{-E_{\mathrm{a}}}{KT}\right), \tag{4}$$

$$u\frac{\partial N}{\partial x} + v\frac{\partial N}{\partial y} = D_{\mathrm{n}}\frac{\partial^2 N}{\partial y^2} - \frac{bW_{\mathrm{c}}}{(C_{\mathrm{w}} - C_\infty)}\left[\frac{\partial N}{\partial y}\frac{\partial C}{\partial y} + N\frac{\partial^2 C}{\partial y^2}\right] + \frac{\rho_{\mathrm{p}}}{\rho\tau_{\mathrm{m}}}(N_{\mathrm{p}} - N). \tag{5}$$

Second phase (for dust particles):

$$\frac{\partial u_{\mathrm{p}}}{\partial x} + \frac{\partial v_{\mathrm{p}}}{\partial y} = 0, \tag{6}$$

$$u_{\mathrm{p}}\frac{\partial u_{\mathrm{p}}}{\partial x} + v_{\mathrm{p}}\frac{\partial u_{\mathrm{p}}}{\partial y} = \frac{K}{m}(u - u_{\mathrm{p}}), \tag{7}$$

$$\rho_{\mathrm{p}}C_{\mathrm{m}}\left(u_p\frac{\partial T}{\partial x} + v_{\mathrm{p}}\frac{\partial T}{\partial y}\right) = \frac{\rho_{\mathrm{p}}C_{\mathrm{m}}}{\tau_{\mathrm{T}}}(T - T_{\mathrm{p}}), \tag{8}$$

$$u_{\mathrm{p}}\frac{\partial C_{\mathrm{p}}}{\partial x} + v_{\mathrm{p}}\frac{\partial C_{\mathrm{p}}}{\partial y} = \frac{1}{\tau_{\mathrm{c}}}(C - C_{\mathrm{p}}), \tag{9}$$

$$u_{\mathrm{p}}\frac{\partial N_{\mathrm{p}}}{\partial x} + v_{\mathrm{p}}\frac{\partial N_{\mathrm{p}}}{\partial y} = \frac{1}{\tau_{\mathrm{m}}}(N - N_{\mathrm{p}}). \tag{10}$$

The adopted conditions on and away from the surface are as follows:

$$\mu_{\mathrm{nf}}\frac{\partial u}{\partial y} = \frac{\partial \sigma}{\partial x} = -\sigma_0\left(\gamma_{\mathrm{T}}\frac{\partial T}{\partial x} + \gamma_{\mathrm{C}}\frac{\partial C}{\partial x}\right), \quad \text{at} \quad y = 0, \tag{11}$$

$$v = 0, \quad T = T_{\mathrm{w}}, \quad C = C_{\mathrm{w}}, \quad N = N_{\mathrm{w}}, \quad \text{at} \quad y = 0, \tag{12}$$

$$u \to U_{\mathrm{e}}(x), u_{\mathrm{p}} \to U_{\mathrm{e}}(x), v_{\mathrm{p}} \to v, \quad \text{at} \quad y \to \infty, \tag{13}$$

$$T \to T_\infty, C_{\mathrm{p}} \to C_\infty, N \to N_\infty, N_{\mathrm{p}} \to N_\infty, \quad T_{\mathrm{p}} \to T_\infty, \quad C \to C_\infty, \quad \text{at} \quad y \to \infty. \tag{14}$$

The Marangoni convection phenomenon can be described by equation (11). This phenomenon has prominent engineering and technology applications.

$$\sigma = \sigma_0[1 - \gamma_T(T - T_\infty) - \gamma_C(C - C_\infty)],$$
$$\gamma_C = -\frac{\partial\sigma}{\partial C}\bigg|_T, \gamma_T = -\frac{\partial\sigma}{\partial T}\bigg|_C. \tag{15}$$

The viscosity that is almost temperature-dependent is given below [34]:

$$\mu^*(T) = \mu_{nf}\left[1 + \epsilon_1\left(\frac{T - T_\infty}{T_w - T_\infty}\right)\right]. \tag{16}$$

The thermal conductivity that is also temperature-dependent is given below [34]:

$$K^*(T) = k_{nf}\left[1 + \epsilon\left(\frac{T - T_\infty}{T_w - T_\infty}\right)\right]. \tag{17}$$

2.2 Similarity transformations

The adopted similarity variables can be composed as follows:

$$u_p = dxg'(\xi), \quad v_p = -(vd)^{0.5}g(\xi). \quad \rho_p = mN, \tag{18}$$

$$u = dxf'(\xi), \quad v = -(vd)^{0.5}f(\xi), \xi = y\left(\frac{d}{v}\right)^{0.5}, \tag{19}$$

$$T(x,y) = T_\infty + (T_w - T_\infty)\theta(\xi),$$
$$T_P(x,y) = T_\infty + (T_w - T_\infty)\theta_P(\xi), \tag{20}$$

$$C(x,y) = C_\infty + (C_w - C_\infty)\phi(\xi),$$
$$C_P(x,y) = C_\infty + (C_w - C_\infty)\phi_p(\xi), \tag{21}$$

$$N(x,y) = N_\infty + (N_w - N_\infty)\Theta(\xi),$$
$$N_P(x,y) = N_\infty + (N_w - N_\infty)\Theta_P(\xi). \tag{22}$$

The terminologies in the above equations are further specified as follows:

$T_w = T_0 + Ax^2$, $C_w = C_0 + Bx^2$, $N_w = N_0 + Dx_2$;
$T_\infty = T_0 + Ex_2$, $C_\infty = C_0 + Fx_2$ and $N_\infty = N_0 + Gx_2$,

where the microorganism gradient coefficients are C and G, the solute gradient coefficients are B and F, and the temperature gradient coefficients are A and E. Now using equations (18)–(22) in governing equations (1)–(14), we obtain the dimensionless equations (as given below).

First phase:

$$\begin{aligned} &A_1(1 + \epsilon_1\theta(\xi))f'''(\xi)((1 - n) + n\mathrm{We}f''(\xi)) \\ &+ A_1\epsilon_1\theta'(\xi)((1 - n)f''(\xi) + n\mathrm{We}(f''(\xi))^2) \\ &+ A_2(f''(\xi)f(\xi) - [f'(\xi)]^2) + \beta_v l(g'(\xi) - f'(\xi)) \\ &+ \lambda^2 + A_3M(\lambda - f'(\xi)) = 0, \end{aligned} \tag{23}$$

$$\begin{aligned} &A_4(\theta''(\xi)(1 + \epsilon\theta(\xi)) + \epsilon(\theta'(\xi))^2 + \frac{4}{3}\mathrm{Rd}\theta''(\xi) \\ &+ A_5\mathrm{Pr}(f(\xi)\theta'(\xi) - 2f'(\xi)\theta(\xi)) \\ &+ \mathrm{Pr}\gamma l\beta_t[\theta_p(\xi) - \theta(\xi)] + \mathrm{PrEc}\beta_v l(g'(\xi) - f'(\xi))^2 \\ &+ \mathrm{PrEc}A_1((1 - n) + n\mathrm{We}f''(\xi))(f''(\xi))^2(1 \\ &+ \epsilon_1\theta(\xi)) + \mathrm{Pr}Q_t\theta(\xi) + \mathrm{Pr}Q_e e^{(-n\xi)} + \mathrm{PrDu}\phi''(\xi) \\ &= 0, \end{aligned} \tag{24}$$

$$\begin{aligned} &\phi''(\xi) + \mathrm{Le}(f(\xi)\phi'(\xi) - 2f'(\xi)\phi(\xi)) \\ &+ \mathrm{Le}l\beta_c[\phi_p(\xi) - \phi(\xi)] - \tau\mathrm{Le}(\phi'(\xi)\theta'(\xi) \\ &+ \phi(\eta)\theta''(\xi)) - \mathrm{RcLe}(1 + \delta\theta(\xi))^m \exp\bigg(\\ &-\frac{E}{1 + \delta\theta}\bigg)\phi(\xi) + \mathrm{Sr}\theta''(\xi) = 0, \end{aligned} \tag{25}$$

$$\begin{aligned} &\Theta''(\xi) - \mathrm{Pe}\,[\Theta'(\xi)\phi'(\xi) + (\Omega + \Theta(\xi))\phi''(\xi)] \\ &+ \mathrm{Lb}(f(\xi)\Theta'(\xi) - 2f'(\xi)\Theta(\xi)) \\ &+ l\beta_m\mathrm{Lb}[\Theta_p(\xi) - \Theta(\xi)] = 0. \end{aligned} \tag{26}$$

Second phase:

$$g(\xi)g''(\xi) - g'(\xi)^2 + \beta_v[f'(\xi) - g'(\xi)] = 0, \tag{27}$$

$$g(\xi)\theta_p'(\xi) - 2g'(\xi)\theta_p(\xi) + \beta_t[\theta(\xi) - \theta_p(\xi)] = 0, \tag{28}$$

$$(g(\xi)\phi_p'(\xi) - 2g'(\xi)\phi_p(\xi)) + \beta_c[\phi(\xi) - \phi_p(\xi)] = 0, \tag{29}$$

$$(g(\xi)\Theta_p'(\xi) - 2g'(\xi)\Theta_p(\xi)) + \beta_m[\Theta(\xi) - \Theta_p(\xi)] = 0. \tag{30}$$

The simplified BCs are

$$A_1f''(0) = -2(1 + \mathrm{Ma}), f(0) = 0, \tag{31}$$

$$f'(\infty) = \lambda, g'(\infty) = \lambda, \quad g(\infty) = f(\infty), \tag{32}$$

$$\theta(0) = 1, \theta(\infty) = 0, \quad \theta_p(\infty) = 0, \tag{33}$$

$$\phi(0) = 1, \phi(\infty) = 0, \quad \phi_p(\infty) = 0, \tag{34}$$

$$\Theta(0) = 1, \Theta(\infty) = 0, \quad \Theta_p(\infty) = 0. \tag{35}$$

2.3 Expression of parameters

We $= \sqrt{2}\Gamma d\left(\frac{d}{\nu}\right)^{1/2}$ – Weissenberg number, Du $= \frac{D_m K_T(C_w - C_\infty)}{C_p C_s(T_w - T_\infty)}$ – Dufour number, $M = \frac{\sigma_f B_0^2}{d\rho_f}$ – magnetic parameter, Ec $= \frac{U_w^2}{C_p(T_w - T_\infty)}$ – Eckert number, Pe $= \frac{b\mathrm{Wc}}{D_n}$ – bioconvection Peclet number, $\lambda = \frac{e}{d}$ – free stream velocity parameter, $\tau_v = \frac{m}{K}$ – dust particle's relaxation time, $\beta_v = \frac{1}{d\tau_v}$ – fluid-particle interaction parameter, $\beta_t = \frac{1}{d\tau_t}$ – thermal interaction parameter, Pr $= \frac{\mu_f C_p}{k_f}$– Prandtl number, $l = \frac{\mathrm{Nm}}{\rho_f}$ – dust

particles mass concentration parameter, Rd = $\frac{4\sigma^* T_\infty^3}{k^* k_f}$ – thermal radiation parameter, Le = $\frac{\alpha}{D_m}$ – Lewis number, $\tau = -\frac{k_1(T_w - T_\infty)d}{\nu_f T_{ref}}$ – thermophoretic parameter, Ω = $\frac{N_\infty}{(N_w - N_\infty)}$ – microorganisms concentration difference parameter, $\beta_c = \frac{1}{d\tau_c}$ – concentration interaction parameter, $\gamma = \frac{C_m}{C_p}$ – specific heat ratio, $Q_T = \frac{Q_0}{d(\rho C_p)_f}$ – temperature dependent heat source parameter, $\delta = \frac{(T_w - T_\infty)}{T_\infty}$ – temperature difference, $Q_e = \frac{Q_1}{d(\rho C_p)_f}$ – exponential dependent heat source parmeter, Ma = $\frac{C_0 \gamma_c}{T_0 \gamma_T}$ – Marangoni ratio parameter, $E = \frac{Ea}{KT_\infty}$ – activation energy parameter, Sr = $\frac{D_m K_T (T_w - T_\infty)}{T_\infty (C_w - C_\infty)}$– Soret number, Lb = $\frac{\alpha}{D_n}$ – bioconvection Lewis number, Rc = $\frac{K_r^2}{d}$– chemical reaction parameter, and $\beta_m = \frac{1}{d\tau_m}$–fluid–particle interaction parameter for bioconvection.

2.4 Dimensionless parameters

The dimensionless analysis of the preeminent parameters is provided in Table 1.

2.5 Physical parameters

The physical parameters of prime interest are given below:

$$\tau_w = \mu_{nf}\left(1 + \epsilon_1\left(\frac{T - T_\infty}{T_w - T_\infty}\right)\right)\left((1-n)\frac{\partial u}{\partial y} + \frac{n\Gamma}{\sqrt{2}}\left(\frac{\partial u}{\partial y}\right)^2\right), \quad (36)$$

Table 2: Actual values of TiO_2 and kerosene oil subject to thermal physical properties (Abbas *et al.* [33], Haneef *et al.* [35])

Properties constituents	c_p (J/kg K)	k (W/m K)	σ $(\Omega m)^{-1}$	ρ (kg/m^3)
TiO_2	686.2	8.9538	2.38×10^{-6}	4,250
Kerosene oil	2,090	0.145	21×10^{-6}	783

Table 3: Physical relations (Abbas *et al.* [32])

Properties	Nanofluid
Dynamic viscosity (μ_{nf})	$A_1 = \frac{\mu_{nf}}{\mu_f} = \frac{1}{(1-\Phi)^{2.5}}$
Density (ρ_{nf})	$A_2 = \frac{\rho_{nf}}{\rho_f} = \left[\left\{\Phi\frac{\rho_{s_1}}{\rho_f} + (1-\Phi)\right\}\right]$
Electrical conductivity (σ_{nf})	$A_3 = \frac{\sigma_{nf}}{\sigma_f} = \left[\frac{\sigma_{s_1}(1+(S-1)\Phi) + (S-1)\sigma_f(1-\Phi)}{\sigma_{s_1}(1-\Phi) + \sigma_f((S-1)+\Phi)}\right]$
Thermal conductivity (k_{nf})	$A_4 = \frac{k_{nf}}{k_f} = \frac{((S-1)k_f + k_{s_1}) - (S-1)\Phi(k_f - k_{s_1})}{(S-1)k_f + k_{s_1}) + \Phi(k_f - k_{s_1})}$
Heat capacitance $(\rho c_p)_{nf}$	$A_5 = \frac{(\rho c_p)_{nf}}{(\rho c_p)_f} = \left[\left\{\Phi\frac{(\rho c_p)_{s_1}}{(\rho c_p)_f} + (1-\Phi)\right\}\right]$

$$\mathrm{Sh}_x = \frac{x q_m}{D_m(C_w - C_\infty)}, \quad \mathrm{Nn}_x = \frac{x q_n}{D_n(N_w - N_\infty)}, \quad C_{fx} = \frac{\tau_w}{\rho_f U_w^2}, \quad \mathrm{Nu}_x = \frac{x q_w}{k_f(T_w - T_\infty)}, \quad (37)$$

$$q_w = -\left[k_{nf}\left(1 + \epsilon\left(\frac{T - T_\infty}{T_w - T_\infty}\right)\right) + \frac{16T_\infty^3\sigma^*}{3k^*}\right]\left.\frac{\partial T}{\partial y}\right|_{y=0}, \quad (38)$$

$$q_m = -D_m\left.\frac{\partial C}{\partial y}\right|_{y=0}, \quad q_n = -D_n\left.\frac{\partial N}{\partial y}\right|_{y=0}, \quad (39)$$

Table 1: Dimensionless analysis of the prime parameters

We = $\sqrt{2}\Gamma d\left(\frac{d}{\nu}\right)^{1/2}$	$\left[\frac{\mathrm{N\,s/m^2}}{\mathrm{N\,s/m^2}}\right] = 1$	Du = $\frac{D_m K_T (C_w - C_\infty)}{C_p C_s (T_w - T_\infty)}$	$\left[\frac{\mathrm{m^2/s}}{\mathrm{m^2/s}}\right] = 1$
$M = \frac{\sigma_f B_0^2}{d\rho_f}$	[kg/m³ × m/s × kg/m³s] = 1	Ec = $\frac{U_w^2}{C_p(T_w - T_\infty)}$	[m/s × J/(kg K) × m/K] = 1
Pe = $\frac{b\mathrm{Wc}}{D_n}$	[m³/s/m × m²/s] = 1	$\lambda = \frac{e}{d}$	[m/s] = 1
$\tau_v = \frac{m}{K}$	[s × m/s × m] = 1	$\beta_v = \frac{1}{d\tau_v}$	[kg/m³ × m/s² × Ns/m²] = 1
$\beta_t = \frac{1}{d\tau_t}$	[W/m² K × m/W/(m K)] = 1	Pr = $\frac{\mu_f C_p}{k_f}$	[kg/m³ × m/s² × Ns/m²] = 1
$l = \frac{\mathrm{Nm}}{\rho_f}$	[kg × m³/kg/m³] = 1	$\tau = -\frac{k_1(T_w - T_\infty)d}{\nu_f T_{ref}}$	$\frac{[\mathrm{LT^{-1}}][\mathrm{K}][\mathrm{L}]}{[\mathrm{L^2T^{-1}}][\mathrm{K}]} = 1$
Ω = $\frac{N_\infty}{(N_w - N_\infty)}$	[m/s × m/m²/s] = 1	$\beta_c = \frac{1}{d\tau_c}$	[kg × m³/kg/m³] = 1
$\delta = \frac{(T_w - T_\infty)}{T_\infty}$	$\frac{[\mathrm{K}]}{[\mathrm{K}]} = 1$	Lb = $\frac{\alpha}{D_n}$	$\frac{[\mathrm{L^{-2}T^{-1}}]}{[\mathrm{L^{-2}T^{-1}}]} = 1$

Table 4: Proposed shape (Abbas *et al.* [33])

Spherical shape	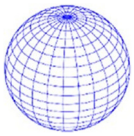
S	3.0

$$C_{fx}(\mathrm{Re}_x)^{-0.5} = A_1(1+\epsilon_1\theta)((1-n)f''(0) + \frac{1}{2}n\mathrm{We}(f''(0))^2), \tag{40}$$

$$\mathrm{Nu}_x(\mathrm{Re}_x)^{-0.5} = -(A_5(1+\epsilon\theta) + \frac{4}{3}\mathrm{Rd})\theta'(0), \tag{41}$$

$$\mathrm{Sh}_x(\mathrm{Re}_x)^{-0.5} = -\phi'(0), \mathrm{Nn}_x(\mathrm{Re}_x)^{-0.5} = -\Theta'(0). \tag{42}$$

The physical characteristics for nanofluids relations are provided in Tables 2–4.

3 RKF-45th scheme

The conditions are set in such a way that dimensionless equation would be solved iteratively.

$$u_1 = f, \quad u_2 = f', u_3 = f'', u_3' = f''', u_4 = g, \quad u_5 = g', u_5' = g'', \tag{43}$$

$$u_6 = \theta, u_7 = \theta', u_7' = \theta'', u_8 = \theta_\mathrm{p}, u_8' = \theta_\mathrm{p}', \quad u_9 = \phi, u_{10} = \phi', u_{10}' = \phi'', \tag{44}$$

$$u_{11} = \phi_\mathrm{p}, u_{11}' = \phi_\mathrm{p}', u_{12} = \Theta, u_{13} = \Theta', \quad u_{13}' = \Theta'', u_{14} = \Theta_\mathrm{p}, u_{14}' = \Theta_\mathrm{p}', \tag{45}$$

$$u_1' = u_2, u_2' = u_3, = u_4, \tag{46}$$

$$u_3' = (-\epsilon_1 u_7 A_1((1-n)u_3 + n\mathrm{We}(u_3)^2) + A_2(u_2^2 - u_1u_3) + L\beta_v(u_2 - u_5) - \lambda^2 - A_3M(\lambda - u_2) \times \frac{1}{((1-n) + n\mathrm{We}u_3)(1+\epsilon_1u_6)A_1}, \tag{47}$$

$$u_4' = u_5, \quad u_5' = u_4^{-1}(u_5^2 + \beta_\mathrm{v}(u_5 - u_2), u_6' = u_7, \tag{48}$$

$$u_7' = (A_4(1+\epsilon u_6) + \mathrm{Rd})^{-1}(A_5(\mathrm{Pr}(2u_2u_6 - u_1u_7) - \epsilon A_4(u_7)^2 + \mathrm{PrL}\gamma\beta_\mathrm{T}(u_6 - u_8) - \mathrm{Pr}LEc\beta_\mathrm{v}(u_5 - u_2)^2 - \mathrm{Ec}A_1(1+\epsilon_1u_6)((1-n) + n\mathrm{We}u_3)(u_3)^2 - M\mathrm{Ec}A_3(u_2)^2 - \mathrm{Pr}Q_\mathrm{t}u_6 - \mathrm{Pr}Q_\mathrm{e}e^{(-n\eta)} - \mathrm{PrDu}u_9'), \tag{49}$$

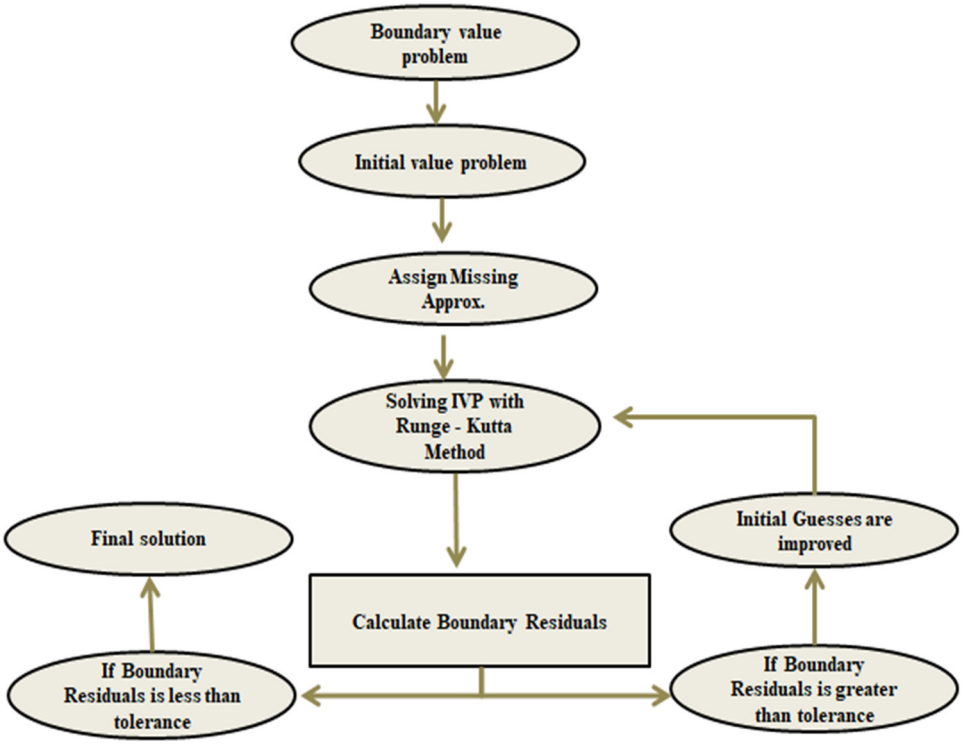

Figure 2: Numerical procedure.

$$u_8' = u_4^{-1}(2u_5u_8 + \beta_T(u_8 - u_6) - \epsilon_2(u_7)^2),$$
$$u_9' = u_{10,}u_{10}' = ((\mathrm{Le}(2u_2u_9 - u_1u_{10}) + \mathrm{Le}\beta_C L(z_9 - z_{11}) + \tau\mathrm{Le}(u_{10}u_7 + u_9u_7') + \mathrm{LeRc}(1 + \delta u_6)^m \exp\left(-\frac{E}{(1 + \delta u_{6)}}\right)u_9 - \mathrm{Le\ Sr}u_{7,}' \quad (50)$$

$$u_{11}' = u_4^{-1}(2u_5u_{11} + \beta_T(u_{11} - u_9)), \quad (51)$$

$$u_{12}' = u_{13,}u_{13}' = ((\mathrm{Lb}\,(2u_2u_{12} - u_1u_{13}) + Lb\beta_m L(u_{12} - u_{14}) + \mathrm{Pe}(u_{13}u_{10} + (\Omega + u_{12})u_{10}'), \quad (52)$$

$$u_{14}' = u_4^{-1}(2u_5u_{14} + \beta_m(u_{14} - u_{12})). \quad (53)$$

The BCs set in simulations are

$$u_1(0) = 0, \quad u_2(0) = \lambda m_1, \quad u_3(0) = -2(1 + Ma), u_4(0) = 0, \quad (54)$$

$$u_5(0) = \lambda m_2, \quad u_6(0) = 1, \quad u_7(0) = m_3, \quad u_9(0) = m_4, \quad u_9(0) = 1, \quad (55)$$

$$u_{11}(0) = m_5, \quad u_{13}(0) = m_6, \quad u_{12}(0) = 1, \quad u_{15}(0) = m_7, \quad u_{17}(0) = m_8. \quad (56)$$

Figure 2 exhibits the numerical procedure based on RKF-45 method.

4 Results and discussion

The analysis of the dominant impacts of the parameters are presented in this section. The parametric ranges are taken from the standard literature [33,36,37], *e.g.*,

$0.1 \le \mathrm{Lb} \le 0.5, 0.1 \le \mathrm{Le} \le 0.5, 0.1 \le E \le 5, 0.1 \le \mathrm{Rc} \le 1.0,$
$0.1 \le \mathrm{Sr} \le 6, 0.5 \le \mathrm{Ma} \le 2.0, 0.1 \le \beta_v \le 0.5, 0.1 \le \beta_t \le 0.5,$
$0.1 \le M \le 4, 2 \le \mathrm{Pr} \le 6.9, 0.1 \le \beta_c \le 0.5, 1 \le \mathrm{Du} \le 1.0,$
$0.1 \le \beta_m \le 0.5,$ and$0.1 \le \mathrm{Pe} \le 1.0.$ r.

Figure 3(a) and (b) illustrate how raising Ma improvises the profiles (velocities and temperatures) for both phases (I and II). The underlying cause of this phenomena is surface variation. The Marangoni effect causes liquid streams to pour, hence it is always followed by an accelerated velocity gradient. These figures show how, when Ma values increase, the temperature, concentration, and microorganism profiles all decrease dramatically. The higher attraction of the liquid to the particles in the geometry causes surface tension to form over the surface. As a result, temperature decreases as surface tension increases. The appearance of the surface molecules causes the thermal gradient to decrease. The temperature gradient lessens as a result.

Figures 4(a) and (b) and 5(a) and (b), respectively, show the effects of β_v, β_t, β_c, and β_m on the prescribed profiles in either case of dust or fluid phases. These figures demonstrate that the microbe, temperature, concentration, and velocity profiles for the particle phase increase considerably with the increase in levels of β_v, β_t, β_c, and β_m, respectively. The fluid phase across the boundary layer is affected by these phenomena quite in the opposite way.

The distribution of the transverse magnetic field will produce a Lorentz force similar to the drag force, which tends to slow the fluid flow in both phases. The momentum boundary layer thickness decreases as M increases. Figure 6(a) and (b) demonstrate, for the two phases (I and II),

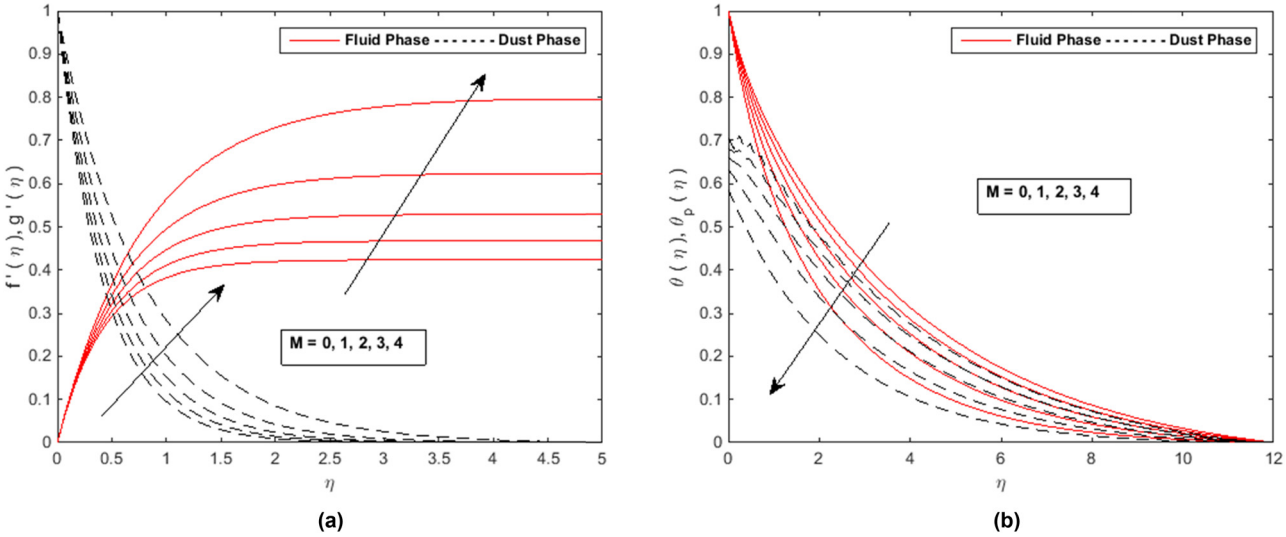

Figure 3: (a) Profiles of $f'(\xi)$ and $g'(\xi)$ with Ma. (b) Profiles of $\theta(\xi)$ and $\theta_p(\xi)$ with Ma.

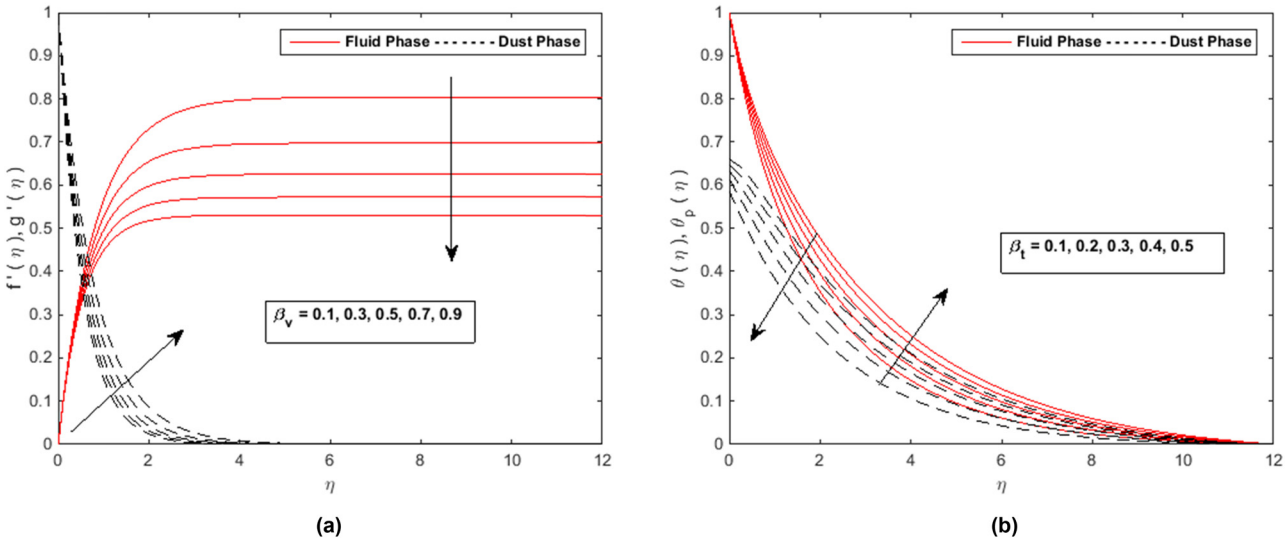

Figure 4: (a) Profiles of $f'(\xi)$ and $g'(\xi)$ with β_v. (b) Profiles of $\theta(\xi)$ and $\theta_p(\xi)$ with β_t.

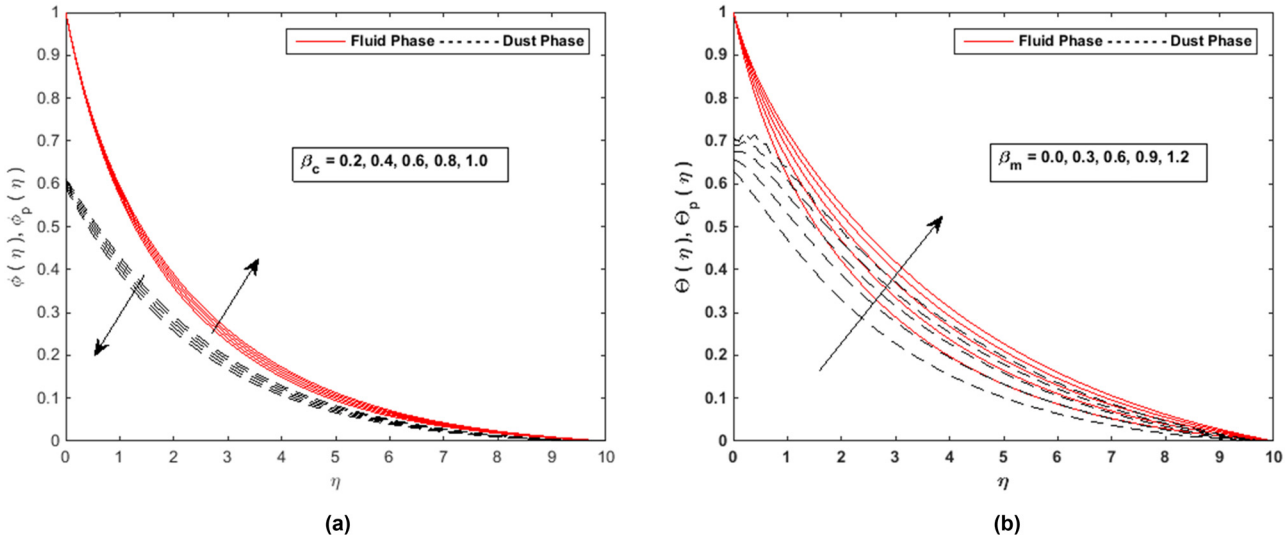

Figure 5: (a) Profiles of $\phi(\xi)$ and $\phi_p(\xi)$ with β_c. (b) Profiles of $\Theta(\xi)$ and $\Theta_p(\xi)$ with β_m.

respectively, the effects of We on $f'(\xi)$, $g'(\xi)$, $\theta(\xi)$, and $\theta_p(\xi)$.

The power law index can be used to explain two different types of fluids: pseudoplastic fluids ($n < 1$) and dilatant fluids ($n > 1$). The velocity profile is reduced as the values of n for the shear thinning phenomenon increases. It is because higher values of the power law index are associated with higher viscosities, which lead to lower fluid velocities. The Weissenberg number is one of the characteristics that also slows fluid velocity. Due to the direct relationship between the Weissenberg number and relaxation time, increasing Weissenberg numbers lengthen the relaxation times and increase resistance to fluid motion, which reduces fluid velocity. As we increase the values of Φ, its effect on velocity starts to disappear. Physically, when the nanoparticles' saturation exceeds that of the nanofluid, the outcome is a denser nanofluid, which causes the velocity to decrease. When the values of Φ are raised, the temperature of the nanofluid and dust phases also rises. Physically, resistance and temperature profiles increase as the concentration of nanoparticles in a tangent hyperbolic fluid increase.

Figure 7(a) and (b) depict the impression of Du and ϵ for the two stages (fluid and dust), respectively. The heat flux brought on by a concentration gradient is referred to as the Dufour effect. The temperature profile behaves

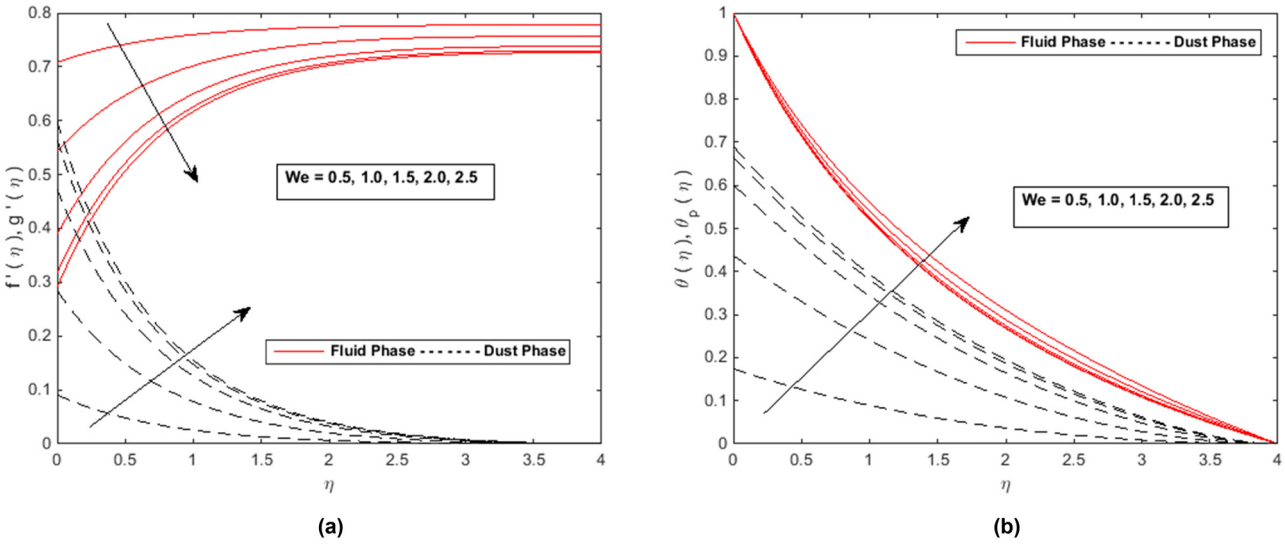

Figure 6: (a) Profiles of $f'(\xi)$ and $g'(\xi)$ with We. (b) Profiles of $\theta(\xi)$ and $\theta_p(\xi)$ with We.

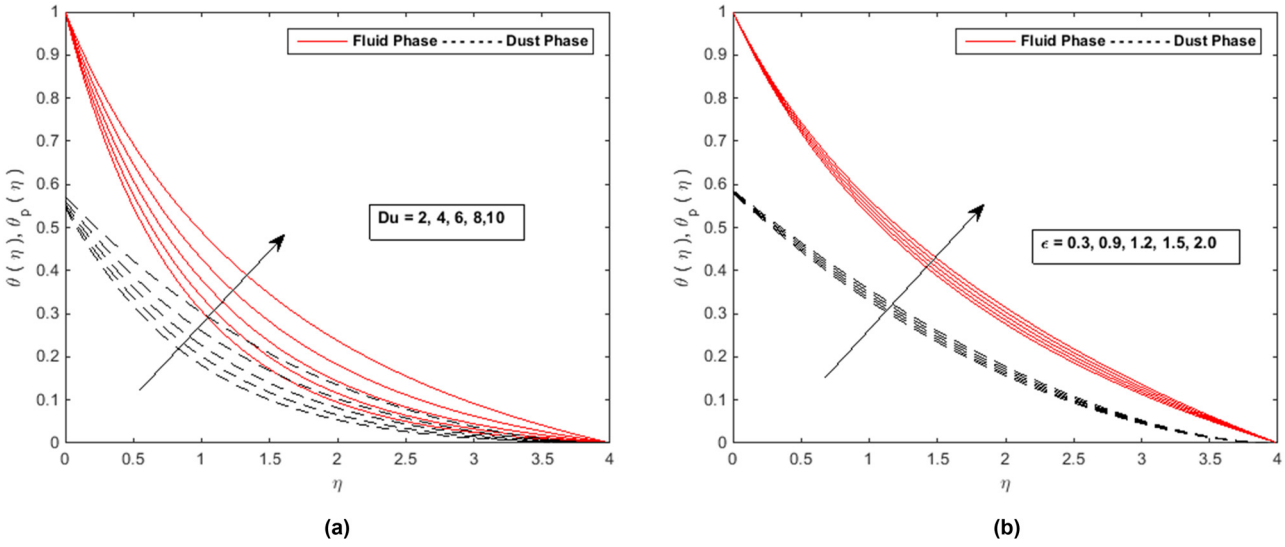

Figure 7: (a) Profiles of $\theta(\xi)$ and $\theta_p(\xi)$ with Du. (b) Profiles of $\theta(\xi)$ and $\theta_p(\xi)$ with ϵ.

negatively when the Dufour effect is missing and stronger when it is present. Along with the Dufour number, the thermal boundary layer thickness drastically increases, and the boundary layer flow appears to be intensifying. As we increase the value of Du, the temperature profiles of the tangent hyperbolic nanofluid and dust phases increase.

Figure 8(a) and (b) illustrate how Ec and Rd affect the profiles $\theta(\xi)$ and $\theta_p(\xi)$ in either case of two phases, respectively. The temperatures of both phases increase as Ec values increase. The Eckert number describes the relationship between the enthalpy and kinetic energy of the flow. It represents the process through which internal energy is produced by applying pressure to a fluid's forces. The thermal boundary layer thickness increases for both phases (I&II) as a result of the increased viscous dissipative heat. As Rd rises, the temperature and thermal boundary layer thickness rise as well. Figure 9(a) and (b) depict the effects of Q_t and Q_e on the temperatures of both phases.

The temperature profiles get better as we increase the values of parameters Q_t and Q_e for the tangent hyperbolic nanofluid and dust phase. Figure 10(a) and (b) show how E and Rc affect the concentration. Figure 10(a) depicts that the concentration is an increasing function of E. The Arrhenius equation demonstrates mathematically that if a

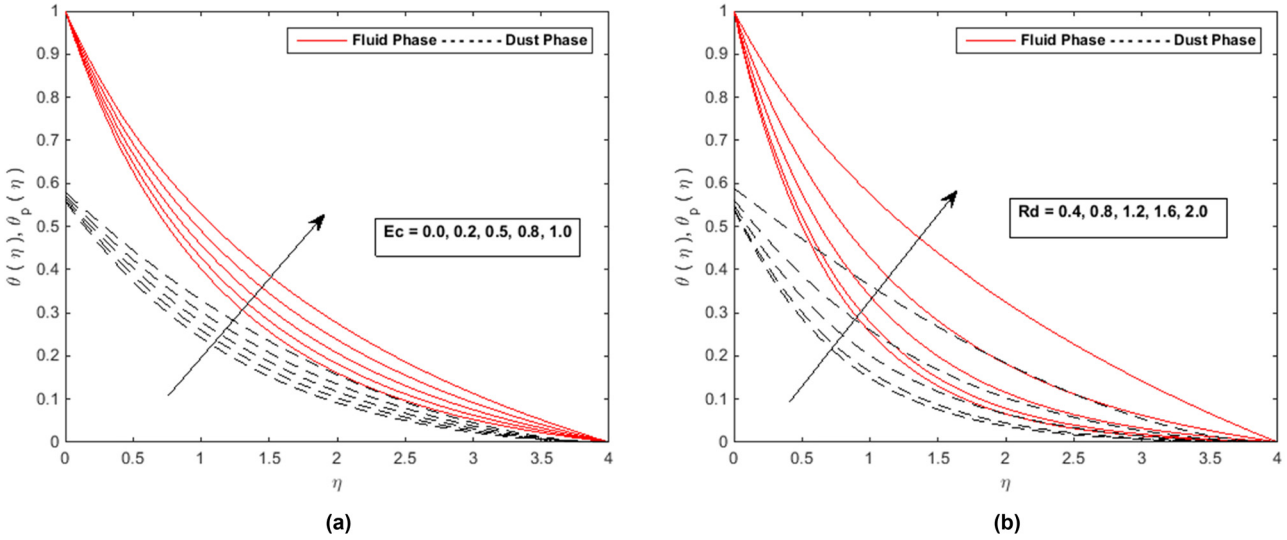

Figure 8: (a) Profiles of $\theta(\xi)$ and $\theta_p(\xi)$ with Ec. (b) Profiles of $\theta(\xi)$ and $\theta_p(\xi)$ with Rd.

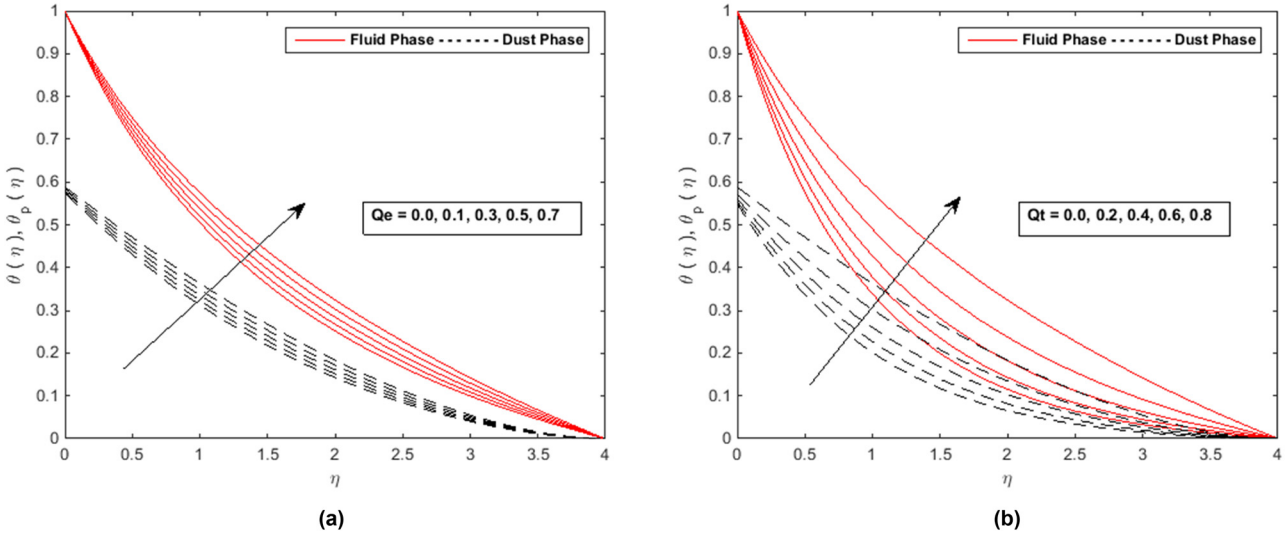

Figure 9: (a) Profiles of $\theta(\xi)$ and $\theta_p(\xi)$ with Q_e. (b) Profiles of $\theta(\xi)$ and $\theta_p(\xi)$ wit Q_t.

chemical reaction slows down because of a reduction in heat, the effect on the concentration profile is greater. When the activation energy increases, the modified Arrhenius mechanism exhibits increasing behavior. Any system's activation energy is acknowledged by the Arrhenius equation. When Rc is increased, the concentration gets decreased.

As the temperature gradient widened, a weaker concentration was seen because of an increase in particle mobility. Figure 11(a) and (b) depict the effects of Le and Lb on the dimensionless temperature and concentration profiles. As Le and Lb increase, it was observed that the concentration and microorganism ($\Theta(\xi)$ and $\Theta_p(\xi)$) profiles decreased. The Lewis number is the reciprocal of the heat to mass diffusivity. The mass diffusivity declines and the thickness of the concentration boundary layer decreases with higher values of Le. Figure 12(a) and (b) show the effects of Ω and Pe on the microorganisms distribution. In both phases (I and II), $\Theta(\eta)$ and $\Theta_p(\eta)$ dropped when Pe and Ω values were increased. A numerical data comparison is depicted in Table 5 which validates the approximate solutions. Tables 6 and 7 comprise the analysis of motile density number and skin friction, respectively.

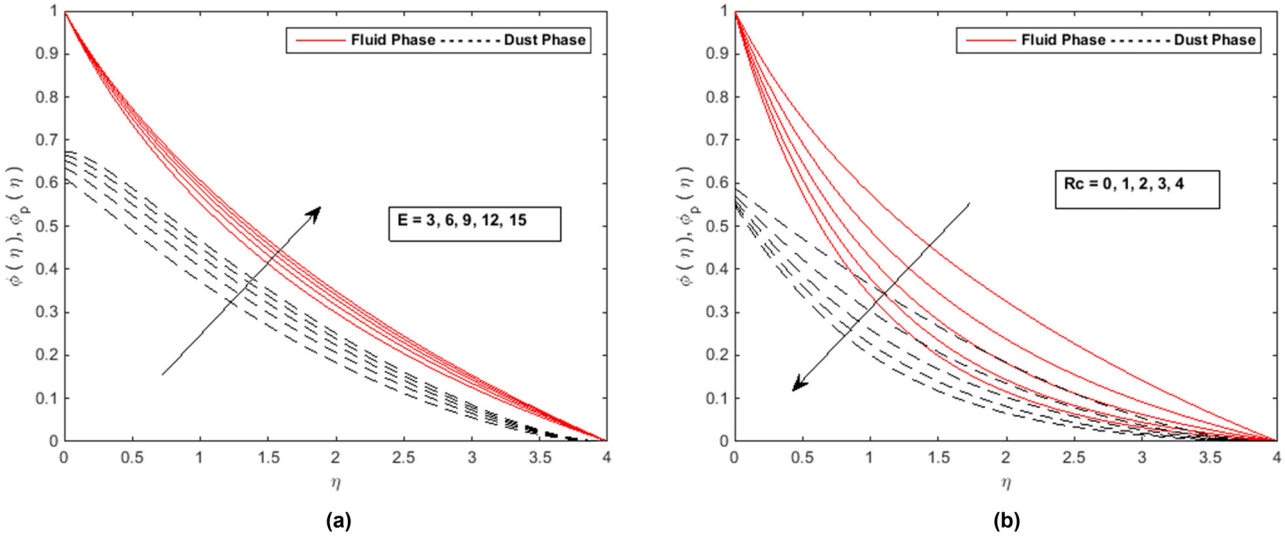

Figure 10: (a) Profiles of $\phi(\xi)$ and $\phi_p(\xi)$ with E. (b) Profiles of $\phi(\xi)$ and $\phi_p(\xi)$ with Rc.

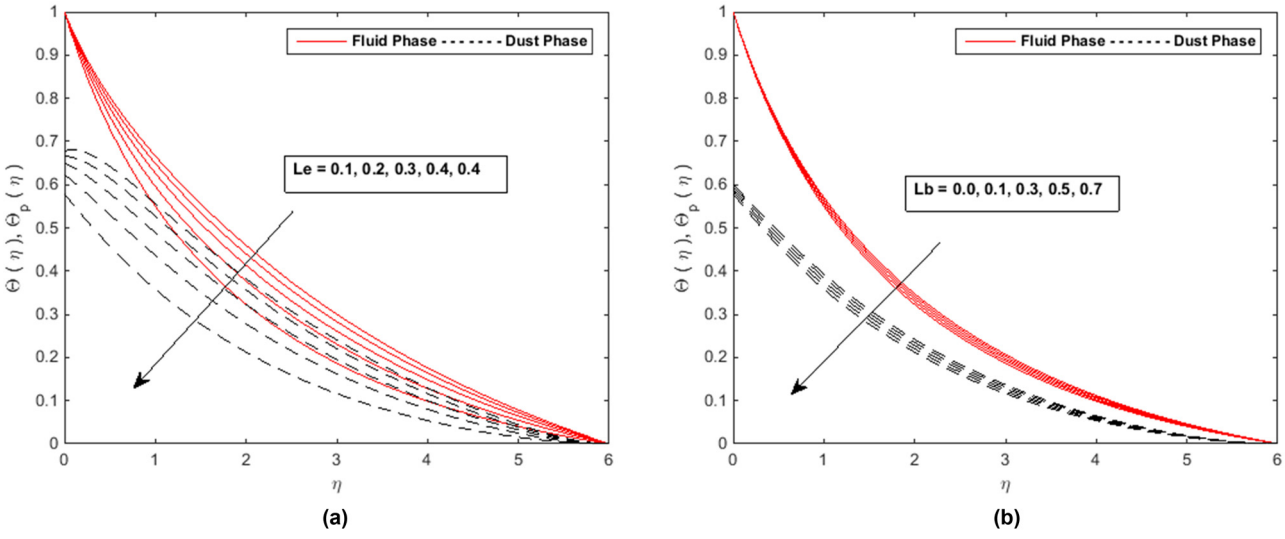

Figure 11: (a) Profiles of $\phi(\xi)$ and $\phi_p(\xi)$ with Le. (b) Profiles of $\Theta(\xi)$ and $\Theta_p(\xi)$ with Lb.

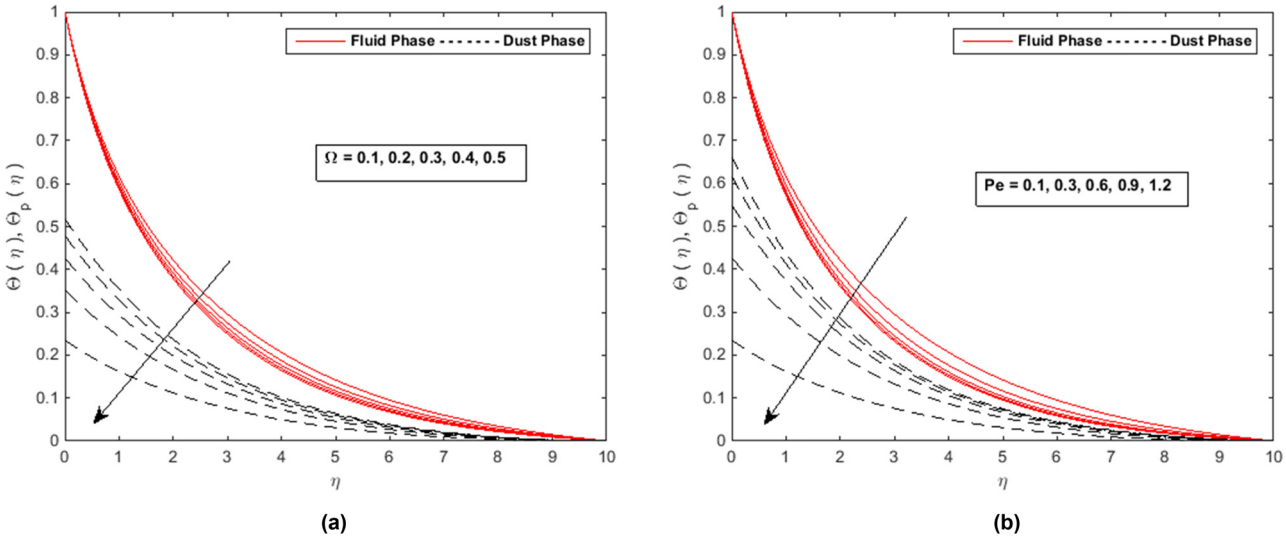

Figure 12: (a) Profiles of $\Theta(\xi)$ and $\Theta_p(\xi)$ with Ω. (b) Profiles of $\Theta(\xi)$ and $\Theta_p(\xi)$ with Pe.

Table 5: Numerical data comparison with the literature [33]

β_m	Sherwood number	
	Sherwood number	**Mamatha *et al.* [33]**
0.1	0.103889	0.103886
0.2	0.126251	0.126246
0.3	0.139274	0.139270

Figure 13 shows the effect of λ on the tangent hyperbolic nanofluid and dust phases. For higher values of λ, the distribution of velocity tends to increase.

Table 6: Change in Nn_x with various parameters

						Microbes density number Nn_x	
L	β_m	Ω	Pe	Sb	Ma	RKF-45	Bvp4c
0.7	0.6	0.1	0.4	0.3	**0.2**	1.921008	1.921004
					0.3	1.922909	1.922918
					0.4	1.923818	1.923827
				0.3		1.920822	1.920825
0.7	0.6	0.1	0.3	**0.4**	0.4	1.920780	1.920775
				0.5		1.920759	1.920756
			0.2			1.920821	1.920817
0.7	0.6	0.1	**0.3**	2.0	0.1	1.920822	1.920820
			0.4			1.920823	1.920825
		0.2				1.920822	1.920820
0.7	0.6	**0.3**	0.3	2.0	0.2	1.938804	1.938808
		0.4				1.948150	1.948153
	0.2					1.920325	1.920330
0.7	**0.3**	0.1	0.3	2.0	0.2	1.918932	1.918942
	0.4					1.918332	1.918340
0.2						1.921695	1.921690
0.3						1.921769	1.921765
0.4	0.6	0.1	0.3	2.0	0.2	1.921842	1.921832

Table 7: Change in C_{fx} with various parameters

						Skin friction C_{fx}	
L	λ	We	β_v	M	Ma	RKF-45th	Bvp4c
			0.1			1.492345	1.492355
0.2	0.5	0.6	**0.2**	0.5	0.7	1.633528	1.633538
			0.3			1.774711	1.774716
				0.1		1.774662	1.774682
0.2	0.5	0.6	0.4	**0.2**	0.7	1.774754	1.774758
				0.3		1.774843	1.774848
					0.3	1.774673	1.774678
					0.4	1.774667	1.774677
0.2	0.5	0.6	0.4	0.5	**0.5**	1.774662	1.774670
0.1	0.5	0.6	0.4	0.5	0.7	2.057052	2.057040
0.2						2.057058	2.057045
0.3						2.057065	2.057058
	0.1					1.774663	1.774660
0.2	**0.2**	0.6	0.4	0.5	0.7	1.774662	1.774658
	0.3					1.774661	1.774650
		0.2				1.774667	1.774660
0.2	0.5	**0.3**	0.4	0.5	0.7	1.774666	1.774654
		0.4				1.774664	1.774650

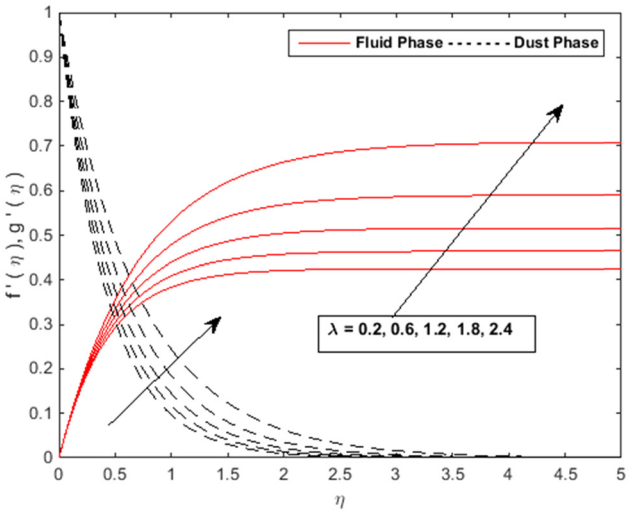

Figure 13: Profiles of $f'(\xi)$ and $g'(\xi)$ with λ.

5 Conclusion

Thermophoretic particle deposition and gyrotactic microorganisms are present in the magneto-Marangoni convective flow of dusty tangent hyperbolic nanofluid over a sheet, and a numerical solution is obtained. The following is the summary of the findings:

- The values of the Weissenberg number lead the heat profiles to increase and the velocity profiles to decrease as we ascend.
- An increase in the Marangoni convection parameter results in an increase in the velocity profiles and skin friction, while the microorganism profiles, heat profiles, and concentration profiles exhibit the opposite behavior for both phases.
- Surface tension greatly depends on the Marangoni number. A liquid's bulk attraction to the particles in the surface layer on its surface causes surface tension.
- As a result, as the surface tension rises, the temperature falls and the bulk magnetism between the surface molecules increases.
- The Soret number demonstrates opposite behavior to that of the nanofluid concentration profiles, which increase as chemical reaction parameter levels do.
- The density of hybrid nanofluid and nanofluid motile bacteria profiles reduces for higher levels of Peclet number. The Peclet number effect causes motile bacteria to swim more quickly, which reduces the thickness of the microorganisms at the surface.
- The value of skin friction increases as the Weissenberg number and the free stream parameter increase, while the magnetic parameter has the opposite effect.
- The Nusselt number at the surface tends to increase with the increase in heat source parameters, but the Dufour number tends to increase in the other direction.
- The Soret number increases the Sherwood number, but the opposite is true when the chemical reaction parameter and the thermophoretic parameter are improved.

6 Future work

Future research should expand on this work by taking into account thermal radiation, Newtonian heating, variable conditions, and trihybrid nanoparticles. These models will be highly helpful in the construction of furnaces, SAS turbines, gas-cooled nuclear reactors, atomic power plants, and unique driving mechanisms for aircraft, rockets, satellites, and spacecraft. In the future, the existing method might be used for a number of physical and technical obstacles [38–47].

Acknowledgments: The authors extend their appreciation to the Deanship of Scientific Research at King Khalid University for funding this work through Large Groups Research Project under grant number RGP.2/168/44.

Funding information: The authors extend their appreciation to the Deanship of Scientific Research at King Khalid University for funding this work through Large Groups Research Project under grant number RGP.2/168/44.

Author contributions: All authors have accepted responsibility for the entire content of this manuscript and approved its submission.

Conflict of interest: The authors state no conflict of interest.

References

[1] Pop I, Ingham DB. Convective heat transfer: Mathematical and computational modelling of tangent hyperbolic fluid and porous media. Amsterdam, Netherlands: Elsevier; 2001 Feb 23.
[2] Akbar NS. Peristaltic flow of a tangent hyperbolic fluid with convective boundary condition. Eur Phys J Plus. 2014 Oct;129:1.
[3] Naseer M, Malik MY, Nadeem S, Rehman A. The boundary layer flow of hyperbolic tangent fluid over a vertical exponentially stretching cylinder. Alex Eng J. 2014 Sep;53(3):747–50.
[4] Salahuddin T, Malik MY, Hussain A, Awais M, Khan I, Khan M. Analysis of tangent hyperbolic nanofluid impinging on a stretching cylinder near the stagnation point. Results Phys. 2017 Jan;7:426–34.
[5] Choi SUS. Enhancing thermal conductivity of fluids with nanoparticles. In development and applications of non-newtonian flow. ASME; 1995. FED-vol. 231/MD-vol. 66. p. 99–I05.
[6] Makinde OD, Aziz A. Boundary layer flow of a nanofluid past a stretching sheet with a convective boundary condition. Int J Therm Sci. 2011 Jul;50(7):1326–32.

[7] Khan N, Nabwey HA, Hashmi MS, Khan SU, Tlili I. A theoretical analysis for mixed convection flow of Maxwell fluid between two infinite isothermal stretching disks with heat source/sink. Symmetry. 2019 Dec;12(1):62.
[8] Khan N, Riaz I, Hashmi MS, Musmar SA, Khan SU, Abdelmalek Z, et al. Aspects of chemical entropy generation in flow of Casson nanofluid between radiative stretching disks. Entropy. 2020 Apr;22(5):495.
[9] Khan N, Al-Khaled K, Khan A, Hashmi MS, Khan SU, Khan MI, et al. Aspects of constructive/destructive chemical reactions for viscous fluid flow between deformable wall channel with absorption and generation features. Int Commun Heat Mass Transf. 2021 Jan;120:104956.
[10] Saffman PG. On the stability of laminar flow of a dusty gas. J fluid Mech. 1962 May;13(1):120–8.
[11] Agranat VM. Effect of pressure gradient of friction and heat transfer in a dusty boundary layer. Fluid Dyn. 1988 Sep;23(5):729–32.
[12] Rahman AM, Alam MS, Chowdhury MK. Thermophoresis particle deposition on unsteady two-dimensional forced convective heat and mass transfer flow along a wedge with variable viscosity and variable Prandtl number. Int Commun heat mass Transf. 2012 Apr 1;39(4):541–50.
[13] Abbas M, Khan N, Shehzad SA. Thermophoretic particle deposition in Carreau-Yasuda fluid over chemical reactive Riga plate. Adv Mech Eng. 2023 Jan;15(1):16878132221135096.
[14] Goren SL. Thermophoresis of aerosol particles in the laminar boundary layer on a flat plate. J Colloid Interface Sci. 1977 Aug;61(1):77–85.
[15] Damseh RA, Tahat MS, Benim AC. Nonsimilar solutions of magnetohydrodynamic and thermophoresis particle deposition on mixed convection problem in porous media along a vertical surface with variable wall temperature. Prog Comput Fluid Dyn Int J. 2009 Jan;9(1):58–65.
[16] Alam MS, Rahman MM, Sattar MA. Effects of variable suction and thermophoresis on steady MHD combined free-forced convective heat and mass transfer flow over a semi-infinite permeable inclined plate in the presence of thermal radiation. Int J Therm Sci. 2008 Jun;47(6):758–65.
[17] Raju CS, Hoque MM, Sivasankar T. Radiative flow of Casson fluid over a moving wedge filled with gyrotactic microorganisms. Adv Powder Technol. 2017 Feb;28(2):575–83.
[18] Chu YM, Al-Khaled K, Khan N, Khan MI, Khan SU, Hashmi MS, et al. Study of Buongiorno's nanofluid model for flow due to stretching disks in presence of gyrotactic microorganisms. Ain Shams Eng J. 2021 Dec;12(4):3975–85.
[19] Hill NA, Bees MA. Taylor dispersion of gyrotactic swimming microorganisms in a linear flow. Phys Fluids. 2002 Aug;14(8):2598–605.
[20] Abdul Latiff NA, Uddin MJ, Bég OA, Ismail AI. Unsteady forced bioconvection slip flow of a micropolar nanofluid from a stretching/shrinking sheet. Proc Inst Mech Eng Part N: J Nanomater Nanoeng Nanosyst. 2016 Dec;230(4):177–87.
[21] Makinde OD, Animasaun IL. Bioconvection in MHD nanofluid flow with nonlinear thermal radiation and quartic autocatalysis chemical reaction past an upper surface of a paraboloid of revolution. Int J Therm Sci. 2016 Nov;109:159–71.
[22] Nisar KS, Faridi AA, Ahmad S, Khan N, Ali K, Jamshed W, et al. Cumulative impact of micropolar fluid and porosity on MHD channel flow: A numerical study. Coatings. 2022 Jan;12(1):93.
[23] Khan N, Hashmi MS, Khan SU, Chaudhry F, Tlili I, Shadloo MS. Effects of homogeneous and heterogeneous chemical features on Oldroyd-B fluid flow between stretching disks with velocity and temperature boundary assumptions. Math Probl Eng. 2020 Apr;2020:1–3.
[24] Kairi RR, Shaw S, Roy S, Raut S. Thermosolutal marangoni impact on bioconvection in suspension of gyrotactic microorganisms over an inclined stretching sheet. J Heat Transf. 2021 Mar;143(3):031201.
[25] Roy S, Raut S, Kairi RR. Thermosolutal marangoni bioconvection of a non-Newtonian nanofluid in a stratified medium. J Heat Transf. 2022 Sep;144(9):093601.
[26] Kairi RR, Roy S, Raut S. Stratified thermosolutal Marangoni bio-convective flow of gyrotactic microorganisms in Williamson nanofluid. Eur J Mechanics-B/Fluids. 2023 Jan;97:40–52.
[27] Roy S, Kairi RR. Bio-Marangoni convection of Maxwell nanofluid over an inclined plate in a stratified Darcy–Forchheimer porous medium. J Magn Magn Mater. 2023 Apr;572:170581.
[28] Magagula VM, Shaw S, Kairi RR. Double dispersed bioconvective Casson nanofluid fluid flow over a nonlinear convective stretching sheet in suspension of gyrotactic microorganism. Heat Transf. 2020 Jul;49(5):2449–71.
[29] Aly EH, Ebaid A. Exact analysis for the effect of heat transfer on MHD and radiation Marangoni boundary layer nanofluid flow past a surface embedded in a porous medium. J Mol Liq. 2016 Mar;215:625–39.
[30] Mat NA, Arifin NM, Nazar R, Ismail F. Radiation effect on Marangoni convection boundary layer flow of a nanofluid. Math Sci. 2012 Dec;6:1–6.
[31] Gevorgyan GS, Petrosyan KA, Hakobyan RS, Alaverdyan RB. Experimental investigation of Marangoni convection in nanofluids. J Contemp Phys (Armen Acad Sci). 2017 Oct;52:362–5.
[32] Abbas M, Khan N, Hashmi MS, Younis J. Numerically analysis of Marangoni convective flow of hybrid nanofluid over an infinite disk with thermophoresis particle deposition. Sci Rep. 2023 Mar;13(1):5036.
[33] Mamatha SU, Ramesh Babu K, Durga Prasad P, Raju CS, Varma SV. Mass transfer analysis of two-phase flow in a suspension of microorganisms. Arch Thermodyn. 2020;41:175–92.
[34] Obalalu AM, Ajala OA, Abdulraheem A, Akindele AO. The influence of variable electrical conductivity on non-Darcian Casson nanofluid flow with first and second-order slip conditions. Partial Differ Equ Appl Math. 2021 Dec;4:100084.
[35] Haneef M, Madkhali HA, Salmi A, Alharbi SO, Malik MY. Numerical study on heat and mass transfer in Maxwell fluid with tri and hybrid nanoparticles. Int Commun Heat Mass Transf. 2022 Jun;135:106061.
[36] Jawad M, Saeed A, Kumam P, Shah Z, Khan A. Analysis of boundary layer MHD Darcy-Forchheimer radiative nanofluid flow with soret and dufour effects by means of Marangoni convection. Case Stud Therm Eng. 2021;23:100792.
[37] Khan MI, Alzahrani F, Hobiny A. Heat transport and nonlinear mixed convective nanomaterial slip flow of Walter-B fluid containing gyrotactic microorganisms. Alex Eng J. 2020;59(3):1761–9.
[38] Gireesha BJ, Mahanthesh B, Thammanna GT, Sampathkumar PB. Hall effects on dusty nanofluid two-phase transient flow past a stretching sheet using KVL model. J Mol Liq. 2018;vol. 256:139–47. doi: 10.1016/j.molliq.2018.01.186.
[39] Hussain SM, Jamshed W. A comparative entropy-based analysis of tangent hyperbolic hybrid nanofluid flow: Implementing finite

difference method. Int Commun Heat Mass Transf. 2021;129:105671.
[40] Sandeep N, Jagadeesh Kumar MS. Heat and mass transfer in nanofluid flow over an inclined stretching sheet with volume fraction of dust and nanoparticles. J Appl Fluid Mech. 2016;9(5):2205–15.
[41] Saleem S, Hussain F, Irfan M, Siddique I, Nazeer M, Eldin SM. Theoretical investigation of heat transfer analysis in Ellis nanofluid flow through the divergent channel. Case Stud Therm Eng. August 2023;48:103140.
[42] Siddique I, Abdal S, Afzal S, Hussain S. Significance of bioconvection for nano-bio film stagnation point flow of micropolar nanofluid over stretching sheet with concentration-dependent transport properties. Waves Random Complex Media. 2023. doi: 10.1080/17455030.2023.2234047.
[43] Yahya AU, Eldin SM, Alfalqui SH, Salamat N, Siddique I, Abdal S. Computations for efficient thermal performance of Go+ AA7072 with engine oil based hybrid nanofluid transportation across a Riga wedge. Heliyon. 2023;9(7):E17920.
[44] Siddique I, Adrees R, Ahmad H, Askar S. MHD free convection flows of Jeffrey fluid with Prabhakar-like fractional model subject to generalized thermal transport. Sci Rep. 2023;13:9289.
[45] Abid F, Alam M, Alamri F, Siddique I. Multi-directional gated recurrent unit and convolutional neural network for load and energy forecasting: A novel hybridization. AIMS Math 8(9):19993–20017.
[46] Mahdy A, Hoshoudy GA. Two-phase mixed convection nanofluid flow of a dusty tangent hyperbolic past a nonlinearly stretching sheet. J Egypt Math Soc. 2019;27:44.
[47] Mahmood R, Majeed AH, Mehmood A, Siddique I. Numerical study of hydrodynamic forces of nonlinear fluid flow in a channel-driven cavity: Finite element-based simulation. Int J Mod Phys B. 2023. doi: 10.1142/S0217979224501844.